Photoelectron imaging of multiply charged anions: Effects of intramolecular Coulomb repulsion and photoelectron kinetic energies on photoelectron angular distributions

Xiao-Peng Xing, Xue-Bin Wang, and Lai-Sheng Wang[a)]
Department of Physics, Washington State University, 2710 University Drive, Richland, Washington 99354, USA and Chemical & Materials Sciences Division, Pacific Northwest National Laboratory, MS K8-88, Richland, Washington 99352, USA

(Received 26 November 2008; accepted 12 January 2009; published online 17 February 2009)

Multiply charged anions possess strong intramolecular Coulomb repulsion (ICR), which has been shown to dictate photoelectron angular distributions (PADs) using photoelectron imaging. Here we report the effects of photoelectron kinetic energies on the PADs of multiply charged anions. Photoelectron images on a series of dicarboxylate dianions, $^{-}O_2C(CH_2)_nCO_2^{-}$ (D_n^{2-}, $n=3-11$) have been measured at two photon energies, 532 and 266 nm. The first photoemission band of D_n^{2-}, which is a perpendicular transition in the absence of the ICR, comes from electron detachment of an O lone pair orbital on the $-CO_2^{-}$ end groups. Recent photoelectron imaging studies at 355 nm show that the PADs of D_n^{2-} peak in the directions parallel to the laser polarization for small n due to the ICR, which directs the outgoing electrons along the molecular axis. The current data show much stronger parallel peaking at 532 nm, but much weaker parallel peaking in the 266 nm data, relative to the 355 nm data. These observations indicate that the ICR has greater influence on the trajectories of slow photoelectrons and much reduced effects on faster photoelectrons. This study demonstrates that the PADs of multiply charged anions depend on the interplay between ICR and the outgoing photoelectron kinetic energies. © *2009 American Institute of Physics*. [DOI: 10.1063/1.3077230]

I. INTRODUCTION

The excess charges in multiply charged anions (MCAs) impart many unique properties to this class of important ions in the gas phase because of the strong intramolecular Coulomb repulsion (ICR). The ICR makes many MCAs unstable as isolated species,[1–6] yet it produces a repulsive Coulomb barrier (RCB) that gives dynamic stability to MCAs,[7–9] even leading to the observation of negative electron binding energies (BEs).[10] Recently, we have shown that the ICR also has major effects on the photoelectron angular distributions (PADs) of MCAs using photoelectron imaging.[11,12] For non-oriented molecules, the PAD with linearly-polarized light can be described by $I(\theta)=c[1+\beta P_2(\cos\theta)]$,[13] where θ is the angle between the laser polarization and the velocity vector of the photoelectron, $P_2(\cos\theta)$ is the second-order Legendre polynomial, β is the anisotropy parameter, and c is a constant proportional to the total ionization cross section. The anisotropy parameter (β), which ranges from -1 for pure perpendicular transitions to +2 for pure parallel transitions, contains the information of the molecular orbitals from which the photoelectrons come from and the dynamics of the photoelectron emission events.[14,15] For MCAs, we found that the outgoing photoelectrons follow the directions of the ICR (Refs. 11 and 12) and the PAD can no longer be described by the above formula. In this article, we report the effects of the photoelectron kinetic energies (KEs) on the PADs of MCAs.

The imaging method was originally developed to record spatial distributions of photodissociation products,[16] but soon applied to photoelectrons from multiphoton ionization of Xe[17] and size-selected cluster anions.[18] With the development of the velocity map imaging technique,[19] photoelectron imaging has evolved into a powerful alternative photoelectron spectroscopy (PES) method over the last several years.[20–25] The advantage of photoelectron imaging lies at its high detection efficiency while yielding PAD information at the same time. In particular, its sensitivity to slow electrons has allowed extremely high resolution photoelectron spectra to be obtained for near zero energy electrons.[26,27] We have recently built a photoelectron imaging system for MCAs. In our initial investigation,[11] we obtained photoelectron images for a series of dicarboxylate dianions $^{-}O_2C(CH_2)_nCO_2^{-}$ (D_n^{2-}, $n=3-11$) using linearly polarized light at 355 nm (3.496 eV) from a Nd:yttrium aluminum garnet (YAG) laser. We showed that the PADs of D_n^{2-} peak in the direction parallel to the laser polarization due to the effects of ICR. But this anisotropy decreases with n and the PDAs reverse to peak at the perpendicular directions for $n\geq 11$ because of the reduced ICR. Using the three structural isomers of benzene dicarboxylates, we have further shown that the PADs not only depend on the magnitudes of the ICR, but also their directions.[12]

The purpose of this article is to describe the details and performances of our imaging system and to report the effects of photoelectron KEs on the PADs of MCAs. We have measured the photoelectron images of D_n^{2-} ($n=3-11$) at 266 nm (4.661 eV) and those of $n=3-5$ at 532 nm (2.331 eV). We observed much stronger peaking in the parallel directions in

a)Author to whom correspondence should be addressed. Electronic mail: ls.wang@pnl.gov.

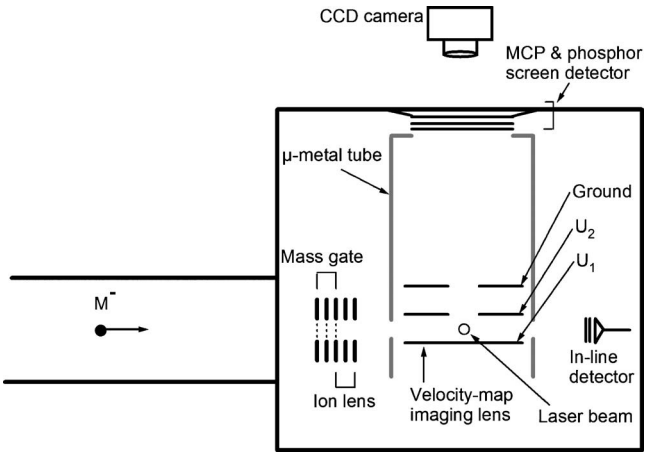

FIG. 1. Schematic of the photoelectron imaging system. M^- indicates the anion beam; U_1 and U_2 are the photoelectron projection voltages.

the PADs at 532 nm. However, the PADs at 266 nm exhibit much less peaking in the parallel directions and for $n>6$ strong peaking in the perpendicular directions was observed. These observations show that the PADs of MCAs strongly depend on the photoelectron KEs, i.e., the photon energies, because the ICR can exert a much stronger effect on the trajectories of slow electrons and a much reduced effect for fast electrons.

II. EXPERIMENTAL METHOD

A. Photoelectron imaging

Figure 1 shows a schematic of our photoelectron imaging analyzer, which includes a velocity-map imaging lens system, a μ-metal shielding tube, a microchannel plate (MCP) and phosphor screen detector assembly, and a charge-coupled device (CCD) camera. The velocity-map imaging lens system consists of three 10 cm diameter copper (oxygen-free high conductivity) plates, which are spaced 2.5 cm apart according to Eppink and Parker.[19] The ground and U_2 plates each have a 2.5 cm diameter opening for the transmission of photoelectrons. The MCP and phosphor screen detector assembly (Chevron™ Model3075FM, PHOTONIS USA, Inc., Sturbridge, MA) with a 75 mm diameter active area is located 20 cm from the center of the photodetachment zone to the surface of the MCP. The detector assembly contains two Imaging Quality Long-Life™ MCPs and a fiber optic phosphor screen with P 47 phosphor mounted to a 20 cm (8.0″) vacuum flange. The anions of interest are selected by a mass gate and focused into the photodetachment zone by an ion lens system under field-free conditions. The photoelectron projection voltages, U_1 and U_2 (variable amplitudes, ~3 μs square pulses) are then switched on 1 μs before the linearly polarized detachment laser is fired. The laser polarization is always parallel to the detector plane. The amplitude of U_1 is varied between −100 and −350 V, depending on the velocities of photoelectrons to be imaged, and the optimized ratio of U_2/U_1 is ~0.7.

The projected positions of photoelectrons on the phosphor screen are recorded by the CCD camera (Model UP-930 from UNIQ VISION, INC., Santa Clara, CA) and saved on a computer. Since the laser polarization is parallel to the surface of the MCP and phosphor screen detector, the original shape of the three-dimensional (3D) electron clouds can be rebuilt through inverse Abel transformation from the recorded two-dimensional images, which are performed using the BASEX program.[28] The electron BE spectra and PADs can be obtained from one slice of the rebuilt 3D electron clouds through the symmetry axis.

B. Generation of multiply charged anions using electrospray ionization

The imaging detector replaces the original magnetic-bottle photoelectron analyzer on our electrospray PES apparatus,[29] which couples an electrospray ion source with a room temperature Paul trap and time-of-flight mass spectrometer. Details of this apparatus have been described in Ref. 29. The preparation of the D_n^{2-} ($n=3-11$) dianions are the same as in our previous studies of these species.[11,30] Briefly, a given D_n^{2-} dianion was produced via electrospray of the respective salt solutions at ~1 mM concentration in a mixed water/methanol solvent. Anions coming from the electrospray source were guided by a radio-frequency quadrupole ion guide into the room temperature Paul trap. Ions were accumulated for ~0.1 s, ejected perpendicularly into a time-of-flight mass spectrometer at a 10 Hz repetition rate, and detected by a set of in-line MCP detector. The D_n^{2-} ions of interest were mass selected before being focused into the photodetachment zone and then detached by a linearly polarized laser beam from a Nd:YAG laser: 266 nm (4.661 eV), 355 nm (3.496 eV), or 532 nm (2.331 eV). The typical detachment laser intensities used are ~1 mJ/cm^2 at 266 nm, ~4.5 mJ/cm^2 at 355 nm, and ~30 mJ/cm^2 at 532 nm for the current experiment. Even at 266 nm, we observed negligible background electron signals [see Fig. 2(a)] and thus no background subtraction was necessary in the current work.

C. Performance and calibrations

Figure 2 shows the photoelectron imaging results of I^- at 266 nm and Br^- at 355 nm, which are used to calibrate the imaging analyzer. For each species, we present the raw image (top in the inset), the sliced image after inverse Abel transformation (bottom in the insert), and the photoelectron BE spectrum obtained by integrating the signals at all angles in the transformed images. The double arrow above the image in the insert indicates the directions of the laser polarization and the intensity scale bar is included next to the raw image of I^- [Fig. 2(a)]. The numbers in each energy spectrum show the energy resolution as full width at half maximum and the corresponding electron KEs are given in the parenthesis. The energy resolution ($\Delta Ek/Ek$) in the I^- spectrum at 266 nm is ~2.5–3.0%, which is comparable to our previous magnetic-bottle photoelectron analyzer.[29] However, the 5 meV resolution for the low KE peak in the Br^- spectrum is much better than the magnetic-bottle instrument because the stray field in the photodetachment zone makes it difficult to achieve good energy resolution for low energy electrons using the magnetic-bottle apparatus.

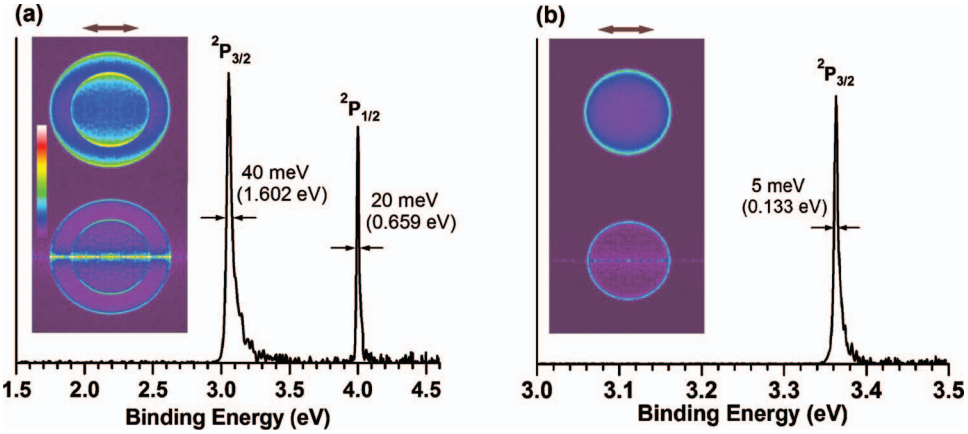

FIG. 2. (Color) Photoelectron spectra for (a) I^- at 266 nm (4.661 eV) and (b) Br^- at 355 nm (3.496 eV) obtained from imaging. The inset in (a) and (b) shows the raw image (top) and the sliced image (bottom) after inverse Abel transformation. The double arrows show the directions of the laser polarization. The relative intensity scale bar is shown on the image of I^-. The numbers in each spectrum show the peak widths at full width at half maximum and the corresponding photoelectron KEs are given in the parentheses.

III. RESULTS

A. Photoelectron Imaging of $^-O_2C(CH_2)_nCO_2^-$ (n=3–11) at 266 nm

Figure 3 compares the symmetrized raw images of D_n^{2-} (n=3–11) at 266 nm with those at 355 nm reported recently.[11] The double arrow shows the laser polarization directions and the intensity scale bar is the same as that given in Fig. 2(a). The ring in each image represents photodetachment transitions and its diameter is proportional to the velocity of the outgoing photoelectrons. The decreasing radius of the ring from D_3^{2-} to D_{11}^{2-} at both photon energies indicates the decreasing electron KEs or increasing electron BEs. The central bright spot appearing in some images come from electrons with zero or near zero KEs. These electrons cannot come from the parent dianions because of the RCB.[30] They are most likely originated from thermionic emissions from the product monoanions that were left with electronic excitations upon photodetachment. The photon energy dependence of the zero energy electron signals is consistent with this interpretation, i.e., these signals are stronger in the 266 nm spectra and they are negligible or very weak in the 532 nm spectra [see Fig. 5(a)] because of the lack of electronic excitation in the product monoanions. The 266 nm laser beam seems to generate a very weak background noise in an area close to the center of the imaging detector. This noise may form a symmetric pattern in the symmetrized image. It is visible in the case of n=3, manifesting itself as the weak feature perpendicular to the laser polarization [Fig. 3(a)] and showing up in the BE spectra around 4 eV [Fig. 4(a)]. For $n>4$, the intensities of the real signals are much stronger and the effect of the noise becomes negligible.

For the images of D_n^{2-} at 266 nm, the outer ring for n =3–6 is nearly isotropic, and starting from n=7 the emission intensity clearly peaks in the direction perpendicular to the laser polarization. The anisotropy observed in the 266 nm images is quite different from that at 355 nm, where the emission intensity peaks in the parallel direction for smaller n.[11] The parallel pattern weakens gradually as the size of the dianion increases and becomes nearly isotropic for $n>8$. Only in the image of n=11 is there a hint of peaking in the perpendicular direction.

After inverse Abel transformation, we obtained the PES spectra in electron BEs and PADs, as shown in Fig. 4, where the current 266 nm data are compared with those at 355 nm, as reported previously.[11] The PES spectra at 266 nm are similar to our previous data obtained using the magnetic-bottle apparatus.[30] A new band (A) at higher binding energy was observed in the 266 nm, that was cut off by the RCB at 355 nm. Compared to the previous magnetic-bottle data, the intensity of the A band in each spectrum appears to be slightly enhanced in the imaging data. In the PAD plot [Figs. 4(b) and 4(c)], the maximum intensity in each case has been normalized to one and the vertical tick represents an increment of 0.2. The horizontal axis (θ) represents the angle between the photoemission direction and the laser polarization. To facilitate comparison at the two photon energies, the energy range used to integrate for the PAD is the same at 266 and 355 nm and it basically covers the main body of the first emission band (X). Because of symmetry, only the top half of the ring (θ from 0° to 180°) is shown in the PAD plots, which are essentially numerical representations of the anisotropy observed in the images shown in Fig. 3. For n=3, the 266 nm PAD peaks slightly in the parallel directions at θ =0° and 180°, whereas for n=4–6 the 266 nm PADs are

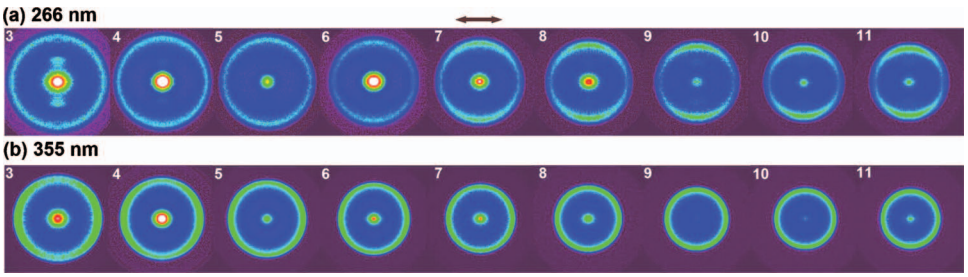

FIG. 3. (Color) Photoelectron images of $^-O_2C(CH_2)_nCO_2^-$ (D_n^{2-}) (n=3–11) at (a) 266 nm compared with those at (b) 355 nm from Ref. 11. The double arrow indicates the directions of the laser polarization. The intensity scale bar is the same as that given in Fig. 2(a). Each image has been symmetrized for inverse Abel transformation.

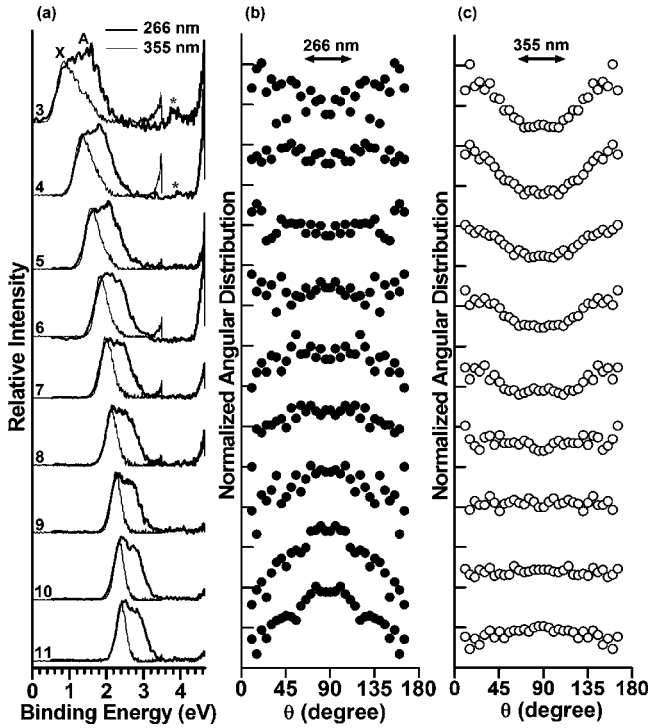

FIG. 4. (a) Photoelectron spectra of $^{-}O_2C(CH_2)_nCO_2^{-}$ (D_n^{2-}) ($n=3-11$) at 266 nm (thicker line) compared with those at 355 nm (thinner line) obtained from the images in Fig. 3. Photoelectron KEs were obtained from the radius (R) of the images $KE \propto R^2$ calibrated by the photoelectron images of Br^- and I^-. The electron BEs were determined by $BE=h\nu-KE$. The photoelectron intensities were obtained by integrating all angles after inverse Abel transformation. The features marked by " *" on the spectra of $n=3$ and 4 at 266 nm come from background noises. PADs for the first band of D_n^{2-} at (b) 266 and (c) 355 nm. The double arrows represent the directions of the laser polarization. The maximum intensity in each plot has been normalized to one. The vertical scale is 0.2 per tick. Because of symmetry, only half of the image from Fig. 3 is plotted ($\theta=0°-180°$).

roughly isotropic, as in the raw images shown in Fig. 3. The 266 nm PADs also reveal quite clearly the perpendicular peaking for $n \geq 7$ at $\theta=90°$.

B. Photoelectron imaging of $^{-}O_2C(CH_2)_nCO_2^{-}$ ($n=3-5$) at 532 nm

As shown previously,[31] the 532 nm photon is below the RCB for all D_n^{2-} dianions. Photoemission can only occur by tunneling through the RCB and there is only enough tunneling probability for $n=3-5$ to allow PES spectra to be observed.[31] The photoelectron images for D_n^{2-} ($n=3-5$) are shown in Fig. 5(a). Indeed, much lower photodetachment cross sections were observed at 532 nm and much higher photon flux had to be used to obtain the presented images (see Sec. II B). The obtained electron BE spectra and the PADs are shown in Figs. 5(b) and 5(c), respectively. The double arrows again indicate the laser polarization directions and the intensity scale bar is the same as that in Fig. 2. For all these three species, we observed very strong peaking in the parallel direction at $\theta=0°$ and 180°. The anisotropy (the minimum in the PADs) is more than 60% in all cases and almost reaches 80% for $n=4$. The PES spectra are similar to

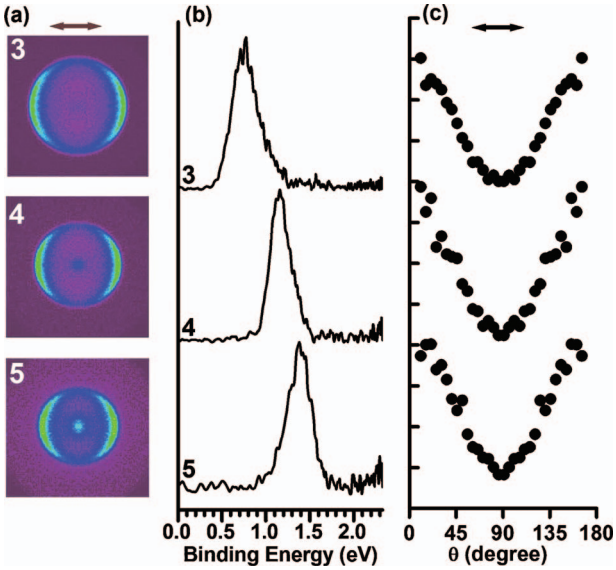

FIG. 5. (Color) (a) Photoelectron images of $^{-}O_2C(CH_2)_nCO_2^{-}$ (D_n^{2-}) ($n=3-5$) at 532 nm (2.331 eV). (b) Photoelectron spectra obtained from the images in (a), and (c) PADs. Each frame is normalized to one and the scale is 0.2 per tick. The arrows represent the laser polarization.

those obtained previously using the magnetic bottle,[31] except that the current spectra appear to be sharper and slightly better resolved.

IV. DISCUSSION

The energy spectra shown in Figs. 4(a) and 5(b) are nearly identical to our previous data obtained using the magnetic-bottle apparatus.[30,31] With increasing chain length in D_n^{2-}, the strength of ICR decreases, which results in higher electron BEs. This effect has been well interpreted in Ref. 30 and here we focus our discussion on the PADs obtained from the imaging experiment.

As we have shown in our recent studies, the PADs of MCAs are dictated by the magnitudes and directions of the ICR, rather than the Cooper–Zare formula. The first photodetachment band in the D_n^{2-} dianions involve photodetachment of O lone pairs on the carboxylate terminal groups,[30] which is a perpendicular transition in the absence of ICR, i.e., the photoelectrons should peak at directions perpendicular to the laser polarization for a singly charged anion.[11] However, as shown in our previous study at 355 nm, the ICR directs the outgoing electrons along the molecular axis, giving rise to the parallel electron distributions for smaller n, as schematically shown in Fig. 6(a). At very small n, the strong ICR results in the strong parallel peaking. As n increases, the magnitude of the ICR decreases and the parallel anisotropy decreases and reverses to peaking in the perpendicular directions for $n=11$. Our current study at 266 and 532 nm demonstrates that the outgoing electron KEs have a profound effect on their trajectories or angular distributions. At 266 nm, the photoelectron KEs for the first detachment band increase by 1.165 eV relative to that at 355 nm. Therefore, the ICR has a much diminished effect on the faster electrons. For example, the PAD for $n=3$ peaks strongly in the parallel directions at 355 nm, whereas at 266 nm the PAD is almost

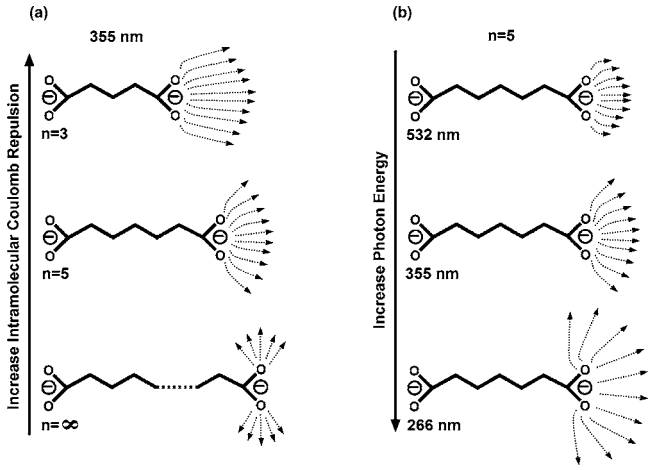

FIG. 6. (a) Schematics illustrating the effect of ICR on the photoelectron trajectories for D_n^{2-} ($n=3$, 5 and ∞) at 355 nm and (b) schematics showing the effect of increasing photon energies or electron KEs on the outgoing electron trajectories for D_5^{2-}.

isotropic. On the other hand, at 532 nm the outgoing electron KEs are reduced by 1.165 eV relative to that at 355 nm and strong parallel peaking was observed in all three D_n^{2-} ($n=3-5$) dianions (Fig. 5).

We use Fig. 6(b) to schematically illustrate the dependence of PADs for D_5^{2-} on photon energies, i.e., photoelectron KEs. The ICR is an intrinsic molecular property, but the outgoing electron KEs are determined by the photon energies. The final PAD is then a result of the interplay between the ICR and the electron KEs. For slow electrons (532 nm), the ICR exerts a much stronger effect, leading to a strong observed parallel peaking along the laser polarization. For fast electrons (266 nm), the effect of the ICR on the electron trajectories is reduced, giving rise to a more isotropic PAD. If the electron KE is much larger than the ICR, we expect that the outgoing electrons would tend to keep their original angular distribution and become less sensitive to the ICR.

For singly charged species or neutral molecules, the PAD is mainly determined by the orbital properties from which the electron is emitted and the dependence of PAD on photon energies is due to the change in the probabilities to generate free electron waves with different quantum numbers.[13–15] However, for MCAs the PAD could be dominated by ICR and the dependence of PAD on photon energies is based on the relative magnitudes of the ICR and the photoelectron KEs. In a very recent report,[12] we have demonstrated that the PADs for MCAs also depend on the direction of the ICR and may yield structural information.

V. CONCLUSIONS

We have described a photoelectron imaging system for the study of MCAs. Photoelectron images for a series of dicarboxylate dianions $^-O_2C(CH_2)_nCO_2^-$ (D_n^{2-}, $n=3-11$) have been obtained at 266 and 532 nm and are compared with previous data at 355 nm to determine the effects of photoelectron KEs on their angular distributions. It was found that the angular distribution is determined by the interplay between the magnitude of the ICR and the electron KEs. The ICR has a much stronger effect on the trajectories of slow electrons and much less effect on fast electrons. Thus, for MCAs it is advantageous to use lower photon energies in order to observe the strongest effect of ICR on the PADs.

ACKNOWLEDGMENTS

We thank Professor M. A. Johnson and his group for valuable discussions and help during the construction of the imaging analyzer and Professor H. Reisler for the BASEX program used for the inverse Abel transformation. This work was supported by the U.S. Department of Energy, Office of Basic Energy Sciences, Chemical Science Division and partly by the National Science Foundation (Grant No. CHE-0749496) and performed at the W. R. Wiley Environmental Molecular Sciences Laboratory, a national scientific user facility sponsored by DOE's Office of Biological and Environmental Research and located at Pacific Northwest National Laboratory, which is operated for DOE by Battelle.

[1] J. Kalcher and A. F. Sax, Chem. Rev. (Washington, D.C.) **94**, 2291 (1994).
[2] M. K. Scheller, R. N. Compton, and L. S. Cederbaum, Science **270**, 1160 (1995).
[3] A. I. Boldyrev, M. Gutowski, and J. Simons, Acc. Chem. Res. **29**, 497 (1996).
[4] G. R. Freeman and N. H. March, J. Phys. Chem. **100**, 4331 (1996).
[5] L. S. Wang and X. B. Wang, J. Phys. Chem. A **104**, 1978 (2000).
[6] A. Dreuw and L. S. Cederbaum, Chem. Rev. (Washington, D.C.) **102**, 181 (2002).
[7] R. L. Hettich, R. N. Compton, and R. H. Ritchie, Phys. Rev. Lett. **67**, 1242 (1991).
[8] X. B. Wang, C. F. Ding, and L. S. Wang, Phys. Rev. Lett. **81**, 3351 (1998).
[9] P. Weis, O. Hampe, S. Gilb, and M. M. Kappes, Chem. Phys. Lett. **321**, 426 (2000).
[10] X. B. Wang and L. S. Wang, Nature (London) **400**, 245 (1999).
[11] X. P. Xing, X. B. Wang, and L. S. Wang, Phys. Rev. Lett. **101**, 083003 (2008).
[12] X. P. Xing, X. B. Wang, and L. S. Wang, J. Phys. Chem. A **113**, 945 (2009).
[13] J. Cooper and R. N. Zare, J. Chem. Phys. **48**, 942 (1968).
[14] K. L. Reid, Annu. Rev. Phys. Chem. **54**, 397 (2003).
[15] A. Sanov and R. Mabbs, Int. Rev. Phys. Chem. **27**, 53 (2008).
[16] D. W. Chandler and P. L. Houston, J. Chem. Phys. **87**, 1445 (1987).
[17] H. Helm, N. Bjerre, D. J. Dyer, D. L. Huestis, and M. Saeed, Phys. Rev. Lett. **70**, 3221 (1993).
[18] J. C. Pinare, B. Baguenard, C. Bordas, and M. Broyer, Phys. Rev. Lett. **81**, 2225 (1998).
[19] A. T. J. B. Eppink and D. H. Parker, Rev. Sci. Instrum. **68**, 3477 (1997).
[20] H. J. Deyerl, L. S. Alconcel, and R. E. Continetti, J. Phys. Chem. A **105**, 552 (2001).
[21] E. Surber and A. Sanov, J. Chem. Phys. **116**, 5921 (2002).
[22] A. V. Davis, R. Wester, A. E. Bragg, and D. M. Neumark, J. Chem. Phys. **118**, 999 (2003).
[23] G. J. Rathbone, T. Sanford, D. Andrews, and W. C. Lineberger, Chem. Phys. Lett. **401**, 570 (2005).
[24] M. A. Sobhy and A. W. Castleman, Jr., J. Chem. Phys. **126**, 154314 (2007).
[25] L. R. Mccunn, G. H. Gardenier, T. L. Guasco, B. M. Elliott, J. C. Bopp, R. A. Relph, and M. A. Johnson, J. Chem. Phys. **128**, 234311 (2008).
[26] A. Osterwalder, M. J. Nee, J. Zhou, and D. M. Neumark, J. Chem. Phys. **121**, 6317 (2004).
[27] S. J. Cavanagh, S. T. Gibson, M. N. Gale, C. J. Dedman, E. H. Roberts, and B. R. Lewis, Phys. Rev. A **76**, 052708 (2007).

[28] V. Dribinski, A. Ossadtchi, V. A. Mandelshtam, and H. Reisler, Rev. Sci. Instrum. **73**, 2634 (2002).
[29] L. S. Wang, C. F. Ding, X. B. Wang, and S. E. Barlow, Rev. Sci. Instrum. **70**, 1957 (1999).
[30] L. S. Wang, C. F. Ding, X. B. Wang, and J. B. Nicholas, Phys. Rev. Lett. **81**, 2667 (1998).
[31] X. B. Wang, C. F. Ding, and L. S. Wang, Chem. Phys. Lett. **307**, 391 (1999).